

# Super-resolution ultrasonic imaging of stiffness variations on a microscale active metasurface

Shane Lani,<sup>1,a)</sup> Karim G. Sabra,<sup>2</sup> and F. Levent Degertekin<sup>2</sup>

<sup>1</sup>Johns Hopkins Applied Physics Laboratory, 11100 Johns Hopkins Road, Laurel, Maryland 20723, USA

<sup>2</sup>George W. Woodruff School of Mechanical Engineering, 801 Ferst Drive, Georgia Institute of Technology, Atlanta, Georgia 30332-0405, USA

(Received 17 November 2015; accepted 12 February 2016; published online 25 February 2016)

Surface acoustic waves propagating over an immersed membrane metasurface, such as an array of capacitive micromachined ultrasonic transducers, can be leveraged to achieve subwavelength focusing and imaging. This is demonstrated numerically and experimentally utilizing a time reversal method on a 2D membrane array at MHz frequencies. The focusing region is a dense metasurface of CMUT membranes with 6.5 MHz resonance frequency that supports a wave field that is evanescent normal to the metasurface and capable of super-resolution along the metasurface. Electrostatically actuated membranes, spatially separate from the focusing region, are used to generate the focused wave field. Subwavelength focusing is demonstrated on the metasurface with a resolution of a single membrane resonator or  $\lambda/5$ . Similar techniques allow for super-resolution imaging of a subwavelength defect or change in the medium of the focusing region. A subwavelength sized imaging target, obtained by altering the stiffness of a single membrane by 1.2%, is shown to be properly imaged with subwavelength resolution. These results pave the way for practical implementation of ultrasonic super-resolution imaging systems using metasurfaces. © 2016 AIP Publishing LLC. [<http://dx.doi.org/10.1063/1.4942752>]

Metamaterials and phononic crystals have been proposed as a platform for super-resolution imaging systems that have resolution smaller than the classical diffraction limit imposed by the Rayleigh criterion.<sup>1,2</sup> Previous metamaterials studies have demonstrated the use of a negative refractive lens to transport the evanescent portion of the waves from one location to the image source on the other side of the lens.<sup>1,3–6</sup> Using these 2D lenses, focal points as small as  $0.14\lambda$  have been achievable where  $\lambda$  corresponds to the acoustic wavelength of the predominate frequency.<sup>7</sup> Another method of deep subwavelength imaging has used tunneling methods based on the Fabry-Perot resonances of engineered structures to capture the evanescent wave field and transport it to where it can be imaged.<sup>8–11</sup>

Subwavelength focusing can also be achieved by leveraging the evanescent field occurring at the interface of two materials between a semi-infinite fluid and a metasurface of resonators. Broadband time reversal subwavelength focusing was demonstrated by Lemoult *et al.* above a metamaterial made of 49 soda cans, each acting as Helmholtz resonator in air.<sup>12</sup> In that study, the evanescent wave field above the soda cans resulted from the acoustic coupling of the resonators through the air and was used to achieve a focusing resolution of  $\lambda/25$  over the array.<sup>12</sup> Continuous excitation can also be used for subwavelength focusing of acoustic waves,<sup>13</sup> but unlike the broadband approach it does not provide the ability to locate the focus location everywhere on the sample which would be required for practical implementation of an imaging system. Broadband time reversal super-resolution imaging has also been demonstrated with electromagnetic

metamaterials<sup>14–18</sup> among others with imaging resolution down to  $\lambda/80$  in the microwave regime.<sup>17</sup> In this work, we demonstrate broadband time reversal focusing and imaging with subwavelength resolution in the ultrasonic regime using a microscale active metasurface in immersion.

The metasurface used in this work is an array of capacitive micromachined ultrasonic transducer (CMUT) membranes in immersion (Fig. 1). This structure supports surface acoustic waves that propagate in two dimensions along the array and are evanescent in the normal direction into surrounding fluid. The dispersion curve of these surface acoustic waves is controlled by the discrete modes of the membrane array and is tunable to 50% of the fundamental frequency as shown in previous work.<sup>19,20</sup> The subwavelength focusing and imaging resolution of  $\lambda/5$  ( $\lambda = 230 \mu\text{m}$  in water) is achieved with the setup shown in Fig. 1(b) (membrane lateral dimensions of  $45 \mu\text{m}$ ,  $10 \mu\text{m}$  spacing, and a center frequency of 6.5 MHz). Since the membranes are electromechanical transducers, these elements can be used to excite or detect the evanescent waves responsible for subwavelength resolution. Unlike previous metasurfaces, this system can be self-characterized by measuring the Green's functions between elements. Hence this CMUT metasurface provides a versatile platform for designing an ultrasonic super-resolution imaging system based on time reversal methods.

Time reversal is a method to refocus sound through a complex or unknown medium. This method has been used extensively to focus sound in complex media such as electromagnetic metamaterials, seismic, shallow water, and ultrasonic environments.<sup>14–18,21–23</sup> Furthermore, the time reversal process has been shown an effective alternative to the inverse filter method for optimizing focusing performance.<sup>24</sup>

<sup>a)</sup>Author to whom correspondence should be addressed. Electronic mail: shane.w.lani@gmail.com

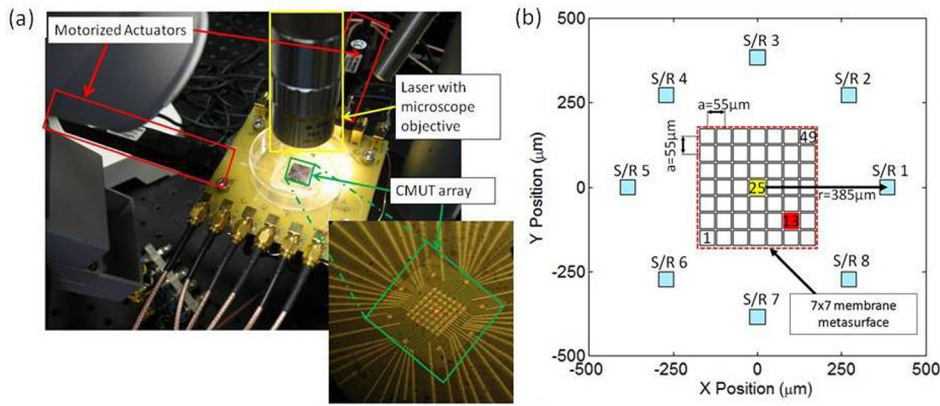


FIG. 1. (a) Experimental setup showing the CMUT membrane metasurface along with a measurement system consisting of motorized actuators for micron accurate positioning and a laser Doppler vibrometer to record displacements at the picometer scale (b) schematic of the control array, comprised of the  $7 \times 7$  membrane metasurface ( $N = 49$ ), and the emitting array, comprised of the exterior Source/Receiver (S/R) elements ( $M = 8$ ).

The steps of time reversal are relatively straightforward and require two arrays: a control array ( $N$  elements) and an emitting array ( $M$  elements), e.g., see Fig. 1(b). First, the desired eventual focal point is chosen within the control array and is excited with an arbitrary waveform noted  $F_0(\omega)$  in the frequency domain. The propagation from the control array to the emitting array with  $M$  elements is determined by the medium and is represented by  $N \times M$  Green's function operator,  $H^T(\omega)$ , where  $T$  denotes the transpose operation.<sup>24</sup> The  $M \times 1$  array of recorded signals by these transducers,  $E_1(\omega) = F_0(\omega)H^T(\omega)$ , contains all of the propagation information from the intended focus location to the emitting array. These  $M$  signals are then time reversed (denoted by  $*$  in the frequency domain) and then retransmitted. These signals then propagate back through the medium,  $H(\omega)$ , and refocus at the location where the original pulse was emitted where the following waveform  $F_1(\omega)$  is received

$$F_1(\omega) = H(\omega)E_1^*(\omega) = H(\omega)(F_0(\omega)H^T(\omega))^*. \quad (1)$$

The time of the focusing is known by the record length used for the time reversal. In essence, the time reversal focusing process stated in Eq. (1) is matched filter. Hence, the waveform  $F_1(\omega)$  is a good approximation of the original waveform  $F_0(\omega)$  with the focused energy concentrated on the intended location in the control array.<sup>12,21,24</sup> If the collective modes of the control array (i.e., the imaging region) are relatively resonant, focusing can be achieved with a small (possible only a single,  $M = 1$ ) number of elements for the emitting array. On the other hand, if the system is very lossy, a larger number  $M$  of emitting elements is required to achieve comparable focusing, a well-known result in the time reversal literature. Hence, the specific number of emitting elements  $M$  is application-dependent.

When time reversal is used iteratively, the result will converge to the inverse filter and can enhance the focus.<sup>24</sup> The iterative method relies on accurately measuring or modeling the Green's function operator,  $H^T(\omega)$ , multiple times. This iterative time reversal focusing technique is used both experimentally and implemented numerically using a semi-analytic boundary element model based upon calculating the mutual radiation impedance between each membrane resonator.<sup>25</sup> This numerical model only requires discretization of the vibrating surfaces (membranes), as opposed to FEM simulations, which require the entire meshing of the surrounding

fluid volume, thus allowing for faster computations and/or the processing of large arrays. The CMUT array surface is modeled as a two dimensional nodal mesh, and for each frequency of interest, a force balance equation is solved for the displacement,  $\{\tilde{u}\}$ , for each node

$$\{\tilde{V}\} = [[K] - \omega^2[M] + j\omega[Z_{mut}]]\{\tilde{u}\}. \quad (2)$$

The force balance encompasses four effects from (1) the electrostatic forcing,  $\tilde{V}$ , (2) the membrane stiffness,  $K$ , (3) the mass,  $M$ , and (4) forces from the fluid in the form of mutual radiation impedance,  $Z_{mut}$ . The mutual radiation impedance is computed by a boundary element method (BEM) which is derived from the Green's function of a baffled point source in a semi-infinite fluid. This mutual radiation impedance term contains the coupling between each membrane and accounts for the evanescent waves above the metasurface.

The modal frequencies, mode shapes, and associated damping can be computed by setting the electrostatic forcing,  $\tilde{V}$ , to zero in Eq. (2) and solving the eigenvalue problem.<sup>20</sup> The dispersion relation and radiation pattern of these modes can also be calculated.<sup>20</sup> In the harmonic regime (i.e., single frequency), the most subwavelength mode occurs when neighboring membrane moves out of phase (i.e., alternating up-down pattern) and thus has an associated wavelength of twice the pitch. However, when using broadband time reversal, all of the modes of the system can be excited at multiple frequencies. This increase in the number of degrees of freedom of the system can result in a focal resolution that is smaller than the most subwavelength mode of the system.<sup>12,16,17</sup>

The CMUT metasurface used in the experiments is shown in Fig. 1. It consists of a dense grid of 7 membranes in both the  $X$  and  $Y$  directions (i.e., a total  $N = 49$  membranes forming the control array). Surrounding the dense grid are  $M = 8$  membranes which act as source/receivers (emitting array) to perform time reversal focusing. All these  $N + M = 57$  membranes have a center frequency of 6.5 MHz and have the same size with a lateral dimension of 45 μm and 10 μm spacing between the membranes of the grid. A full view of the experimental array mounted on a printed circuit board (PCB) with the laser Doppler vibrometer (LDV) head (Polytech OFV-534), a 10× microscope objective, and electrical connections is shown in Fig. 1(a) along with a close up of the array. The LDV was used to record the small displacements of the membranes, but with enhanced

electronics, CMUTs would be able to detect these waves electrically.<sup>26,27</sup> With this experimental configuration, the laser vibrometer can focus to spot sizes of  $3\text{ }\mu\text{m}$  diameter and measure displacements up to a frequency of 24 MHz with  $0.1\text{ pm}/\sqrt{\text{Hz}}$  resolution at 100% reflectivity.<sup>28</sup>

Time reversal and iterative time reversal experiments and simulations were performed to focus at two different membranes, one at the center and the other one located off-center in the lower-right corner of the control array. For the sake of conciseness, only the iterative time reversal results (which have improved focusing over regular time reversal in terms of side lobes as expected<sup>12,18</sup>) are shown in this section. For iterative time reversal focusing, the Green's function operator  $H(\omega)$ , accounting for the propagation between each of the  $M=8$  sensors in the emitting array to each of the  $N=49$  sensors in the control array, was measured experimentally. This was accomplished by exciting each element of the emitting array with a 60 V, 50 ns, unipolar pulse and subsequently measuring the displacement on each membrane in the  $7\times 7$  control array. Figure 2 shows the experimental (Figs. 2(a) and 2(c)) and simulation (Figs. 2(b) and 2(d)) results of subwavelength focusing with five iterations of time reversal. In all cases, the normalized membrane displacement at the focal time (20  $\mu\text{s}$  of time reversal used) is shown in logarithmic scale. Results for the experiments and the numerical simulations agree very well in terms of focus size, side lobe structure, and levels. The differences between the simulation and the experiments are primarily due to the small manufacturing imperfections in the micromachined membranes which affect the modes of the systems and the dispersive propagation.<sup>20</sup> The focusing results illustrates that the acoustic energy is focused to the lateral dimensions of a single membrane, i.e., here a focal spot of  $\lambda/5$ . This focal spot, while only shown here at two locations, can be located at any of the  $N=49$  membranes in the control array.

Beyond focusing applications, this membrane metasurface can be used for super-resolution imaging. The proposed technique uses a baseline and perturbed system to image the

location of a small perturbation as commonly used in structural health monitoring and medical imaging.<sup>21,29–31</sup> In this letter, as a proof of concept, a single subwavelength imaging target is used by altering the stiffness of a single membrane and then is imaged with time reversal methods.

The imaging process using the CMUT metasurface is detailed as follows. The first step is to take a baseline measurement by pulsing one membrane of the imaging grid (center membrane, denoted with yellow in Fig. 1(b)) with a 5 V, 50 ns, unipolar pulse and capturing the signals on the 8 transducers of the emitting array. Then the system is perturbed to mimic a subwavelength defect by changing the DC bias to 10 V of one membrane (13th membrane denoted with red in Fig. 1(b)) which corresponds to 1.2% reduction in stiffness. Then the perturbed system is probed again by pulsing from the center membrane and capturing 8 signals on each element of the emitting array. At this point, each emitting element has captured two waveforms from a center membrane pulse Fig. 3(a) (shown for just S/R 1), one as the baseline pulse (blue line) and a second with the defect introduced (red line). These signals are then subtracted to obtain a difference signal as shown in Fig. 3(b) which contains information about the perturbation, i.e., the difference between the two propagation media. The difference signal is time reversed and transmitted by the emitting array elements while using the unperturbed (or baseline) propagation system to perform the back-propagation. The time reversal displacement results in an image with energy being focused on the array at the location of the defect but at an unknown focusing time. The time of focusing on the defect can be found without *a priori* knowledge of the defect location by finding the maximum displacement in the recorded signals on the control array. Figs. 3(c) and 3(d) show the imaging results as the acoustic energy is focused back to the defect's location for both the experiments and simulation. Note that the imaged defect is a single membrane with subwavelength dimensions ( $\lambda=230\text{ }\mu\text{m}$  in water) and the image also resolves the defect's location with super-resolution.

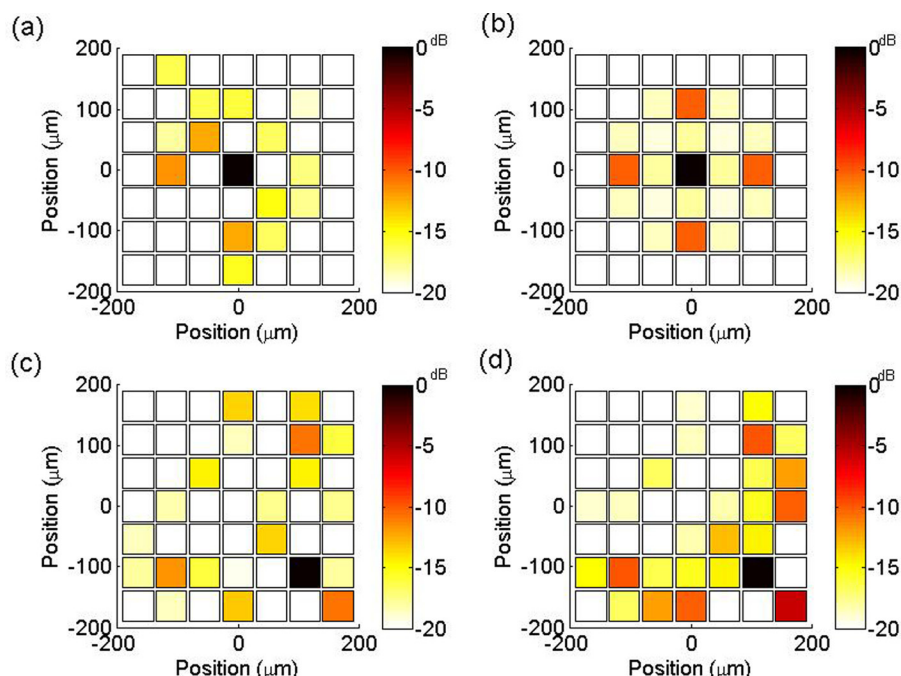


FIG. 2. Iterative time reversal focusing results showing the displacement of all membranes in the control array at the expected focal time for focusing to the center membrane with (a) experimental and (b) simulated results. Iterative focusing to an arbitrarily selected off-center membrane for (c) experimental and (d) simulated results.



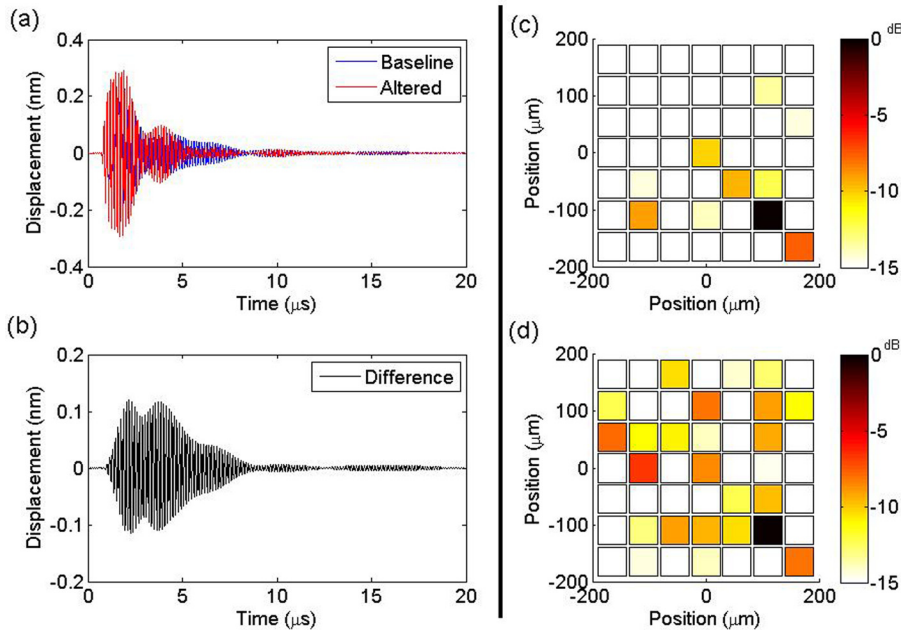


FIG. 3. (a) Displacement of the first exterior S/R membrane when the center membrane in the grid is pulsed with a baseline array (blue line) and when the 13th membrane (see Fig. 1(b)) is biased at 10 V (red line) (b) difference of the two displacements from Fig. 3(a). This signal is then time reversed and played back by each of the  $M=8$  S/R membranes to generate a focal spot at the defective membrane with both the (c) experimental and (d) simulated imaging results plotted as normalized displacement in dB scale.

To explore the limitations of this imaging method, simulations were run for varying defect strengths. Figure 4 illustrates the effects of the imaging system for different changes in the stiffness. There were two aspects of the imaging that were examined. The first was how small or large of a defect could be detected. Defect changes that are too small would not register as a change to the system while large changes can be too drastic for the difference method to work as it requires a linear perturbation of the system. The second aspect examined was the quality of the final image in terms of membrane displacement and the largest side lobe displacement.

Figure 4(a) examines the effect of changing the defect strength as it affects the difference of signals (Fig. 3(b)). The metric observed was an energy ratio calculated based on the following formula for a given defect magnitude, where  $T_R$  represents the duration of the time-reversed system which in this case is  $20 \mu s$

$$E_{ratio} = \frac{\int_0^{T_R} (s_{baseline}(t) - s_{altered}(t))^2 dt}{\int_0^{T_R} (s_{baseline}(t))^2 dt} = \frac{\int_0^{T_R} (s_{difference}(t))^2 dt}{\int_0^{T_R} (s_{baseline}(t))^2 dt}. \quad (3)$$

For small defects, this energy ratio was found to increase relative to the baseline. At defect strengths above 25% change, the energy ratio does not continue to increase. This is due to the propagation system changing too drastically between the baseline and perturbed systems, possibly in a nonlinear manner. This illustrates the relative effectiveness of the difference method of imaging and its limitations. Note that the one set of energy ratios is larger than the rest and is due to the fact that S/R 8 (Fig. 1(b)) lies directly along the path of the defect and the activated center membrane. These results suggest that the difference method can be used to monitor incremental changes in the control array where baseline recordings can be obtained frequently.

Another way to characterize the effects of different defect strength is to examine the properties of the image such as the displacement of the focus and the level of the maximum side lobe in the refocused image. Again similar to the results of the energy ratio of the signal, there is an increase in the image quality with increased displacement of the focal spot (Fig. 4(b)). It is seen that the side lobes increase similarly, so in the end the image contrast remains fairly constant.

This near-field imaging system can potentially image discrete subwavelength targets that exist directly on the

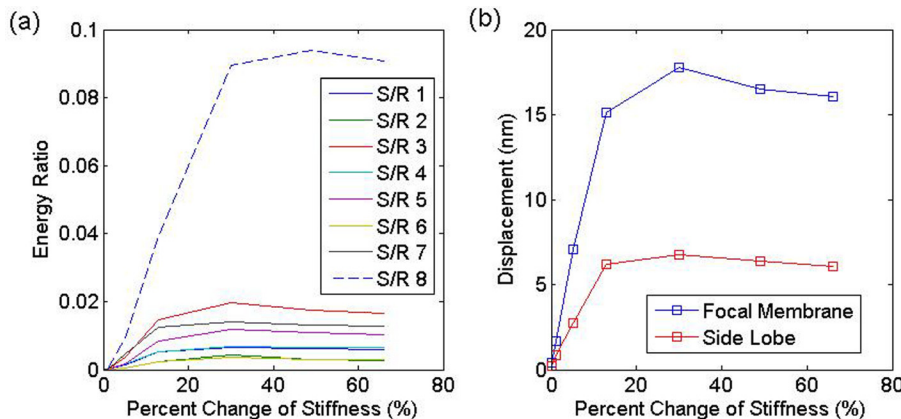


FIG. 4. Imaging effects of different magnitude defects in the metasurface (a) energy of the difference ratio between the baseline and perturb system for each of the 8 S/R locations. (b) Image displacement of the focal membrane (defect location) and the displacement of the largest side lobe for different defects.

metasurface as they would have effects similar to the stiffness change considered here.<sup>18</sup> The presence of imaging targets, such as biological cells, directly on the array surface would affect the propagation and modes of the metasurface in two different ways. First, the imaging targets would alter the static displacement and effective stiffness of each membrane that the target covers. Second, the target would disturb the propagation of the evanescent waves (and to a lesser extent the bulk waves) that travel directly above the metasurface. Hence, a system that can sense these perturbations on the metasurface could image relevant objects with high resolution, as compared to diffraction limited systems, but using much lower ultrasonic frequencies.

These results demonstrated the utility of metasurfaces for subwavelength imaging in immersion and pave the way for practical implementation of super-resolution imaging systems. The demonstration uses the iterative time reversal method implemented on a tunable metasurface to obtain acoustic focusing with a resolution of  $\lambda/5$ . This focus can be achieved to any membrane in the control array of  $7 \times 7$  (Ref. 12) for the selected configuration. Future work will optimize the time reversal focusing process by designing novel array layouts that have superior focusing and subsequent imaging resolution. The subwavelength focusing can be extended to smaller focal spots when the membrane lateral size is reduced while keeping the same resonant frequency.<sup>12,16,20</sup> Enhanced resolution could thus potentially be achieved by using smaller membranes as permitted by manufacturing capabilities. Furthermore, the imaging results presented show that a single subwavelength defect can be localized by using a membrane metasurface and time reversal. The current implementation is limited to localizing one defect which is only slightly different from the original system and is sensitive to changes as small as 1.2% of the original structure. Future modeling and experimental work will examine how relevant objects, such as biological cells, immediately above the array can affect the super-resolution imaging performance.

The authors would like to thank Evren Arkan and Amir Pirouz for fabrication of the metasurfaces in addition to Laurence Jacobs and David Torello for their help with the experimental setup. This work was supported by NSF grant (No. ECCS-1202118).

<sup>1</sup>J. B. Pendry, "Negative refraction make a perfect lens," *Phys. Rev. Lett.* **85**, 3966–3969 (2000).

<sup>2</sup>A. Neice, "Methods and limitations of subwavelength imaging," *Adv. Imaging Electron Phys.* **163**, 117–140 (2010).

<sup>3</sup>M. Ambati, N. Fang, C. Sun, and X. Zhang, "Surface resonant states and superlensing in acoustic metamaterials," *Phys. Rev. B* **75**, 195447 (2007).

<sup>4</sup>H. Su, A. Zhou, X. Xu, and G. Hu, "Experimental study on acoustic sub-wavelength imaging of holey-structured metamaterials by resonant tunneling," *J. Acoust. Soc. Am.* **135**, 1686–1691 (2014).

<sup>5</sup>M. Yang, G. Ma, Z. Yang, and P. Sheng, "Coupled membranes with doubly negative mass density and bulk modulus," *Phys. Rev. Lett.* **110**, 134301 (2013).

<sup>6</sup>N. Kaina, F. Lemoult, M. Fink, and G. Lerosey, "Negative refractive index and acoustic superlens from multiple scattering in single negative metamaterials," *Nature* **525**, 77–81 (2015).

<sup>7</sup>H. Jia, M. Lu, X. Ni, M. Bao, and X. Li, "Subwavelength imaging through spoof surface acoustic waves on a two-dimensional structured rigid surface," *Appl. Phys. Lett.* **103**, 103505 (2013).

<sup>8</sup>Z. Lin, X. Guo, J. Tu, J. Cheng, J. Wu, and D. Zhang, "Acoustic focusing of sub-wavelength scale achieved by multiple Fabry-Perot resonance effect," *J. Appl. Phys.* **115**, 104504 (2014).

<sup>9</sup>F. Liu, F. Cai, S. Peng, R. Hao, M. Ke, and Z. Liu, "Parallel acoustic near-field microscope: A steel slab with a periodic array of slits," *Phys. Rev. E* **80**, 026603 (2009).

<sup>10</sup>D. R. Smith, "How to build a superlens," *Science* **308**, 502–503 (2005).

<sup>11</sup>Y. Zhou, M.-H. Lu, L. Feng, X. Ni, Y.-F. Chen, Y.-Y. Zhu, S.-N. Zhu, and N.-B. Ming, "Acoustic surface evanescent wave and its dominant contribution to extraordinary acoustic transmission and collimation of sound," *Phys. Rev. Lett.* **104**, 164301 (2010).

<sup>12</sup>F. Lemoult, M. Fink, and G. Lerosey, "Acoustic resonators for far-field control of sound on a subwavelength scale," *Phys. Rev. Lett.* **107**, 064301 (2011).

<sup>13</sup>A. A. Maznev, G. Gu, S. Sun, J. Xu, N. Fang, and S. Zhang, "Extraordinary focusing of sound above a soda can array without time reversal," *New J. Phys.* **17**, 042001 (2015).

<sup>14</sup>G. Lerosey, J. de Rosny, A. Tourin, and M. Fink, "Focusing beyond the diffraction limit with far-field time reversal," *Science* **315**, 1120–1122 (2007).

<sup>15</sup>F. Lemoult, G. Lerosey, J. de Rosny, and M. Fink, "Resonant metalenses for breaking the diffraction barrier," *Phys. Rev. Lett.* **104**, 203901 (2010).

<sup>16</sup>F. Lemoult, M. Fink, and G. Lerosey, "Revisiting the wire medium: An ideal resonant metalens," *Waves Random Complex Media* **21**, 591–613 (2011).

<sup>17</sup>F. Lemoult, M. Fink, and G. Lerosey, "Far-field sub-wavelength imaging and focusing using a wire medium based resonant metalens," *Waves Random Complex Media* **21**, 614–627 (2011).

<sup>18</sup>F. Lemoult, M. Fink, and G. Lerosey, "A polychromatic approach to far-field superlensing at visible wavelengths," *Nat. Commun.* **3**, 889 (2012).

<sup>19</sup>S. Lani, M. W. Rashid, J. Hasler, K. G. Sabra, and F. L. Degertekin, "Capacitive micromachined ultrasonic transducer arrays as tunable acoustic metamaterials," *Appl. Phys. Lett.* **104**, 051914 (2014).

<sup>20</sup>S. Lani, K. G. Sabra, and F. L. Degertekin, "Modal and transient analysis of membrane acoustic metasurfaces," *J. Appl. Phys.* **117**, 045308 (2015).

<sup>21</sup>G. Derveaux, G. Papanicolaou, and C. Tsogka, "Time reversal imaging for sensor networks with optimal compensation in time," *J. Acoust. Soc. Am.* **121**, 2071–2085 (2007).

<sup>22</sup>M. Fink and C. Prada, "Acoustic time-reversal mirrors," *Inverse Probl.* **17**, R1–R38 (2001).

<sup>23</sup>W. A. Kuperman, W. S. Hodgkiss, H. C. Song, T. Akal, C. Ferla, and D. R. Jackson, "Phase conjugation in the ocean: Experimental demonstration of a time reversal mirror," *J. Acoust. Soc. Am.* **103**, 25–40 (1998).

<sup>24</sup>M. Tanter, J.-F. Aubry, J. Gerber, J.-L. Thomas, and M. Fink, "Optical focusing by spatio-temporal inverse filter. I. Basic principles," *J. Acoust. Soc. Am.* **110**, 37–47 (2001).

<sup>25</sup>C. Meynier, F. Teston, and D. Certon, "A multiscale model for array of capacitive micromachined ultrasonic transducers," *J. Acoust. Soc. Am.* **128**, 2549–2561 (2010).

<sup>26</sup>G. Gurun, P. Hasler, and F. L. Degertekin, "Frontend receiver electronics for high frequency monolithic CMUT-on-CMOS imaging arrays," *IEEE Trans. Ultrason. Ferroelectr. Freq. Control* **58**, 1658–1668 (2011).

<sup>27</sup>S. Lani, S. Satir, G. Gurun, K. G. Sabra, and F. L. Degertekin, "High frequency ultrasonic imaging using thermal mechanical noise recorded on capacitive micromachined transducer arrays," *Appl. Phys. Lett.* **99**, 224103 (2011).

<sup>28</sup>See <http://www.polytec.com> for "DD-300 24 MHz displacement decoder" (last accessed January 23, 2016).

<sup>29</sup>F. Gustafsson, *Adaptive Filtering and Change Detection* (Wiley, New York, 2000).

<sup>30</sup>I. A. Veres, T. Berer, O. Matsuda, and P. Burgholzer, "Focusing and sub-wavelength imaging of surface acoustic waves in a solid-air phononic crystal," *J. Appl. Phys.* **112**, 053504 (2012).

<sup>31</sup>J. Tian, *Molecular Imaging: Fundamental and Applications* (Springer, New York, 2013).